Oxidative Cleavage of Vicinal Diols Catalyzed by Monomeric Fe-Sites Inside MFI Zeolite

Philipp Treu,[a] Bidyut Bikash Sarma,[a, b] Jan-Dierk Grunwaldt,[a, b] and Erisa Saraçi*[a, b]

The oxidative cleavage of vicinal diols to carboxylic acids was investigated over heterogeneous Fe/MFI catalysts in aqueous medium, with green oxidant H_2O_2 and in mild reaction conditions. High conversions and selectivities (X = 90%, S = 79%) were achieved for the oxidative cleavage of ethylene glycol. Further substrates were also tested broadening the relevance of this catalyst. The employment of non-noble and abundant Fe as the active metal and the MFI-type zeolite as support has a clear advantage over the presently used homogeneous or noble metal-based catalysts. A combination of complementary characterisation techniques with catalytic results is used to show that monomeric Fe species inside zeolite MFI are the active sites for the oxidative cleavage of C—C bonds of vicinal diols. The recyclability of the catalyst and reaction mechanism were also studied.

Introduction

Biomass is a renewable and abundant carbon-neutral resource for sustainable production of chemicals, among which organic acids are very important and widely used fine chemicals.[1] Vicinal diols are commonly found in biomass derived polyols or created *via* epoxidation and subsequent hydrolyzation of C—C double bonds, which are also highly abundant in biomass waste materials i.e. ligno-cellulosic biomass or unsaturated fatty acids.[2] Molecules containing a vicinal diol function can undergo a carbon-carbon bond cleavage, oxidizing each carbon of the vicinal diol to an aldehyde or carboxylic acid. This often leads to highly attractive chemicals.[3] Oxidative cleavage of carbon-carbon bond of vicinal diols has been conducted using stoichiometric amounts of strong oxidizing agents e.g. periodates or lead salts.[4] However, the use of stoichiometric reagents leads to high amounts of waste, which encourages the employment of a catalyst. Several works in literature have reported the use of molecular catalysts, like iron salts,[5] polyoxometalates,[6] or homogeneous vanadium complexes,[7] for the oxidative carbon-carbon bond cleavage of bio-derived vicinal diols. These reactions typically result in formation of e.g., formic acid, a highly demanded commodity chemical.[8] However, separation of the molecular entities from the reaction mixture, use of toxic solvents, high pressure O_2, etc., makes these approaches costly and difficult to implement in larger scale. The utilization of more benign solvents and oxidants, as well as heterogeneous catalysts for this process would offer a more sustainable alternative for obtaining carboxylic acids from biomass.[9] Using H_2O_2 as oxidant allows to conduct the reaction at ambient pressures, simplifying the procedure. The use of H_2O_2 also increases the sustainability index[10], as H_2O_2 can be obtained by direct synthesis from green hydrogen and oxygen[11] or *via* electrolysis.[12] In comparison, the use of molecular oxygen, often requires high pressures to attain an adequate reaction rate.[6,13] Some heterogeneous catalysts have been reported for the C—C bond cleavage, but they are based on precious and/or scarce metals.[14]

Iron is one of the most abundant metals on earth's crust, also being the only 3d metal, next to Ti, which is not considered to face scarcity in the future.[15] Fe is known to catalyze oxidative transformations in the presence of molecular oxygen or H_2O_2 and widely studied to mimic biological systems.[16] Crotti *et al.*[5] showed oxidative cleavage of glycerol to formic acid, using molecular Fe^{III}-salts and H_2O_2. Moreover, previous research has shown that monomeric/dimeric Fe species located in zeolite micropores are effective redox catalyst, able to selectively reduce NO_x in presence of NH_3.[17,18] These redox active Fe-sites have also been used in fine chemistry, e.g., the oxidation of benzene to phenol,[19] for which the extra framework Fe sites on MFI were reported to be the active sites. In another study, Fe(III)-O-radicals and Fe(IV) have been speculated to be the active sites.[20] The oxidation potential of Fe/MFI catalyst has been further reported in the oxidation of methane using H_2O_2, which led to methane activation and C—H bond cleavage at mild temperatures.[21,22,23] Further applications that benefit from the high activity of Fe/MFI catalysts are, e.g., (de)/hydrogenation,[24] dehydration,[25] and other oxidation reactions,[26] as well as higher alcohol[27] and Fischer-Tropsch synthesis.[28] Most of the literature assumes that mononuclear

[a] P. Treu, Dr. B. B. Sarma, Prof. J.-D. Grunwaldt, Dr. E. Saraçi
Institute of Catalysis Research and Technology
Karlsruhe Institute of Technology
Hermann-von-Helmholtz-Platz 1
76344 Eggenstein-Leopoldshafen (Germany)
E-mail: erisa.saraci@kit.edu
[b] Dr. B. B. Sarma, Prof. J.-D. Grunwaldt, Dr. E. Saraçi
Institute for Chemical Technology and Polymer Chemistry
Karlsruhe Institute of Technology
Kaiserstraße 12
76137 Karlsruhe (Germany)

Fe-species confined within the zeolite micropores are the catalytically active sites.[29,30,31]

In this study, we describe the first-time use of Fe/MFI catalysts in the oxidative carbon-carbon bond cleavage of the renewable vicinal diols. Ethylene glycol (EG) was used as model bio-derivable substrate for the systematic study of the catalyst activity and mechanism of the oxidative cleavage reaction. By varying the amount of Fe on the MFI zeolite, the role of different Fe-species on the catalytic activity was investigated. The stability and reusability of the catalyst were also examined. Additionally, the oxidative capabilities of the Fe/MFI system were investigated for larger substrates and bio-derived polyols, broadening the capability of Fe/MFI as catalyst for biomass valorization.

Results and Discussion

Catalysts characterization

The textural properties and measured Fe-loading of all catalysts are shown in Table 1. Elemental analysis showed that the Fe-loading corresponded to the aimed values. Fe impurities (0.04 wt%) were observed in the commercial HMFI55 zeolite, which is not uncommon for technical zeolites.[32] The high BET surface area of zeolites was generally retained after incorporation of Fe. The BET surface area and pore volume slightly decreased upon increasing Fe-loading, probably due to formation of bulkier Fe-species causing some pore blocking. However, in the XRD patterns (Figure S2) no Fe_2O_3 reflections were visible, even for the 5.0Fe/HMFI55, which suggests high dispersion of Fe species. All catalyst samples, including an in-house synthesized Fe-free HMFI50, displayed the characteristic XRD pattern of MFI-type zeolites.[33] SEM images (Figure S3) also confirm the coffin-shaped crystal morphology of the commercial and synthesized zeolites, with similar length of about three microns.[33]

To evaluate the Fe-species, solid-state diffuse reflectance UV-vis spectroscopy (DR-UV-vis) of all the catalysts was performed (Figure 1). Absorption bands centered at 210 nm and 278 nm are representative of tetrahedral and octahedral iron species, respectively, often denoted as monomeric Fe^{3+}-sites.[34] Absorption bands at around 360 nm correspond to dimeric and oligomeric Fe-sites, while the broad band at around
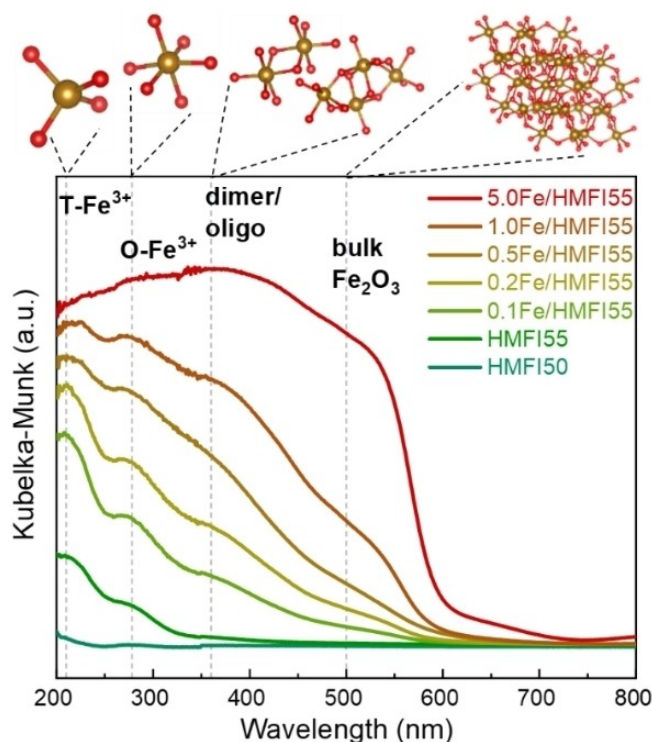

Figure 1. Diffuse reflectance UV-vis spectra of Fe/HMFI55 catalysts. Corresponding FeO_x structures are shown on top of the graph for illustration. T = tetrahedral; O = octahedral. Absorption wavelength positions of various Fe-species are shown by the dotted lines inside the graph.

510 nm corresponds to bulk Fe_2O_3.[17,18,21,22,29,34,35] Deconvolution results of these peaks, shown in Table S1 and Figure S4, revealed that for Fe-loading of up to 0.2 wt% (0.2Fe/HMFI55), monomeric-like Fe-species were dominating. With increasing Fe-loading more oligomeric and bulk Fe-species were formed, as also suggested by the decrease in surface area (see Table 1). The absence of Fe-impurities in the in-house synthesized HMFI50, was confirmed by the UV-vis spectrum with no significant bands visible, whereas commercial HMFI55 showed low bands of monomeric iron from the Fe impurities present (Table 1). Note, however, that assignment of single-site/monomeric species is often demanding.[36]

To elucidate the oxidation state and coordination of Fe, further investigation was carried out by X-ray absorption spectroscopy. For the catalyst with the lowest Fe content (0.1 wt%) and the HMFI55 support, the data quality and signal-to-noise ratio was insufficient for adequate analysis, hence we focused on samples with a Fe content above 0.2 wt%. The XANES spectra at the Fe K-edge in Figure 2 show that for all samples the features around the white line are similar to α-Fe_2O_3 (hematite) reference, confirming an oxidation state of +3, also seen in the UV-vis spectra. In the samples with high Fe-loading (1.0Fe/HMFI55 and 5.0Fe/HMFI55), the shape of the white line resembles more that of the hematite reference, than in the low loaded samples (0.2Fe/HMFI55 and 0.5Fe/HMFI55), indicating more oligomeric/bulk FeO_x species at higher Fe-

Table 1. Structural and elemental analysis of all catalysts by nitrogen physisorption and ICP-OES.

Sample	BET surface area [m²/g]	Micropore volume [cc/g]	Fe (wt %)
Commercial HMFI55	428	0.158	0.04
0.1Fe/HMFI55	414	0.154	0.11
0.2Fe/HMFI55	414	0.154	0.17
0.5Fe/HMFI55	415	0.154	0.44
1.0Fe/HMFI55	410	0.152	0.84
5.0Fe/HMFI55	362	0.128	4.26
HMFI50	–	–	0.00
0.5Fe/HMFI50	–	–	0.49

ChemCatChem

Full Papers
doi.org/10.1002/cctc.202200993
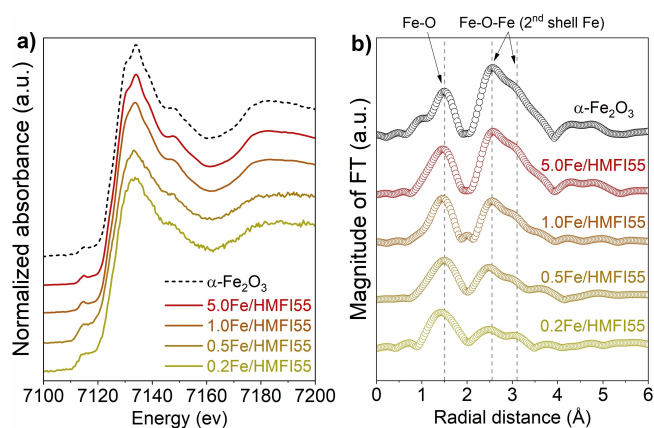
Chemistry Europe
European Chemical
Societies Publishing

Figure 2. a) Normalized XANES spectra and b) Furier-transformed EXAFS spectra at the Fe K-edge for the different Fe/HMFI catalysts and α-Fe_2O_3 (hematite) as reference. Dotted lines in b) highlight the features for the 1st shell Fe—O and 2nd shell Fe—Fe interactions.

loadings and more monomeric FeO_x species at lower Fe-loadings, in very good agreement with results from UV-vis.[17,37]

The oxidation state and geometry of the average Fe-site can be derived from the analysis of the pre-edge region, at about 10 eV below the Fe K-absorption edge. In addition, absorption in the pre-edge region corresponds to a quadrupolar $1s \rightarrow 3d$ electronic transition, which is less intense for Fe-sites with higher symmetry.[38,39] Hence, octahedrally coordinated Fe-sites, which exhibit inverse symmetry unlike tetrahedrally coordinated Fe-sites, show a weaker pre-edge absorption compared to tetrahedral Fe-sites. The pre-edge peak at around 7114.6 eV which is more intense for 0.2Fe/HMFI55 and 0.5Fe/HMFI55 therefore indicates higher amounts of tetrahedral Fe-sites compared to the samples with higher Fe-loading (1.0Fe/HMFI55 and 5.0Fe/HMFI55).[21,39] This is in agreement with UV-vis spectroscopy data, where we could observe higher fractions of octahedral Fe^{3+} and lower of tetrahedral Fe^{3+} with increasing Fe-loading.

The Fourier transformed EXAFS spectra of the Fe/MFI samples and the hematite reference are shown in Figure 2b. All Fourier-transformed EXAFS spectra (Figure 2b) showed a main feature at 1.50 Å (without phase-correction), corresponding to the first shell interaction of Fe—O, also present in the α-Fe_2O_3 reference. The second prominent feature present at 2.55 Å, is either representative for a second shell Fe—O—Fe scattering[21] or a backscattering by Al or Si of the zeolite framework.[40] However, its increase with increasing Fe-loading suggests that the feature indeed corresponds to more Fe—O—Fe contributions from dimeric or oligomeric iron species present in the high Fe-loaded samples.[41] Additionally, a shoulder at the Fe—Fe-backscattering peak appears at 3.00 Å similar to α-Fe_2O_3. Hence, this is also representative of Fe—O—Fe interactions, indicating higher amounts of cluster formation at higher loadings.[41] Analysis of the EXAFS region in k-space (Figure S5) also showed growing similarities to the α-Fe_2O_3 reference with increasing Fe-loading, coming from the formation of Fe_xO_y dimers, oligomers and α-Fe_2O_3 nanoparticles with increasing Fe-loading.

To investigate the oxidation state at reaction conditions, we also conducted XANES experiments at the Fe K-edge under *in-situ* conditions. The white line position and intensity in the XANES spectra (Figure S6) were preserved when the catalyst was measured alone, in contact with H_2O_2 and under reaction conditions with $H_2O_2 + EG$, suggesting that the oxidation state of Fe(III) remains stable at reaction conditions.

The energy-dispersive X-ray spectroscopy (EDS) mapping of 0.1Fe/HMFI55 shown in Figure 3 displays the high dispersion of Fe-sites with little to no agglomeration on the zeolite support. This is also confirmed by the STEM analysis (Figure S7) which show no visible iron oxide clusters for the lower Fe loadings (0.1 and 0.2 wt% Fe), indicating well-dispersed sub nanometer Fe-species, in agreement with UV-vis and XAS results. Similarly, for 0.5 wt% Fe and higher formation of Fe_2O_3 clusters with particle sizes from 50 up to 100 nm for 5.0Fe/HMFI55 was observed.[21]

Oxidative cleavage of ethylene glycol

Ethylene glycol (EG) was chosen as the simplest model compound for bio-derived vicinal diols, in order to obtain distinct structure-activity relationships and insights into the reaction mechanism. To the best of our knowledge, Fe/MFI catalysts have not been previously investigated for this transformation. All Fe/MFI catalysts showed very good activity and selectivity for the oxidative C—C bond cleavage of EG, with formic acid being the main product (Figure 4a). Table S2 and S3 show catalytic results after 2 hours of reaction time and close to iso-conversion, respectively. Among all the synthesized catalysts, 0.2Fe/HMFI55 showed a very good selectivity of 89% at a conversion of 80% after only 2 h of reaction time. The parent HMFI55 also showed satisfactory catalytic activity (Figure 4a), which is due to the Fe impurities (0.04 wt%). This iron in the technical catalyst is known to mainly be present in its monomeric form.[17,18] To verify our hypothesis that Fe is indeed the active metal, we synthesized HMFI50 with similar structural
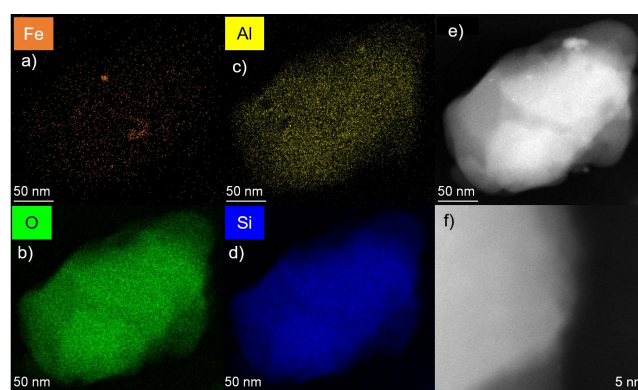

Figure 3. a-d) STEM-EDS mapping for 0.1Fe/HMFI55. e) high-angel annular dark-field (HAADF) STEM image, corresponding to elemental maps. f) High resolution HAADF-STEM image of 0.1Fe/MFI. Si = blue, O = green, Al = yellow, Fe = red.
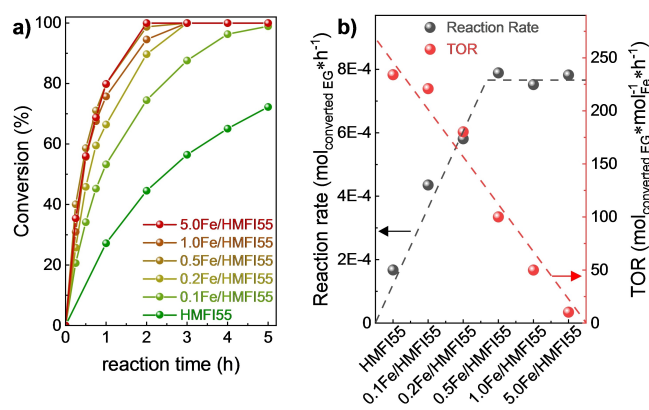
ChemCatChem

Full Papers
doi.org/10.1002/cctc.202200993

Chemistry Europe
European Chemical
Societies Publishing

Figure 4. a) Conversion of EG to formic acid over time on HMFI55 with varying Fe-loading. b) Comparison of reaction rates and TOR for catalysts with different Fe-loadings. Dashed lines serve as guide for the eyes. Reaction conditions: $n_{EG} = 0.715$ mmol; $n_{H2O2} = 3.6$ mmol; $V_{H2O} = 10$ ml; $m_{cat} = 100$ mg; $T = 323$ K. k has been calculated at interpolated reaction time for $X = 50\%$.

properties as the commercial sample (Figure S3) with non-detectable Fe-contamination (Table 1). The synthesized zeolite showed no relevant catalytic activity under the same reaction conditions (Table S2) confirming that Fe, even in minute impurity amounts, plays a significant role in the catalytic activity. Subsequent impregnation of in-house synthesized HMFI50 with 0.5 wt% Fe led to a significant increase of the activity with formic acid yield of 57%. The lower yield here compared to that of 0.5Fe/HMFI55 might be mainly due to structural differences of the zeolite supports, i.e. incomplete crystallization of MFI50 (Figure S2). Kinetic experiments with different content of Fe suggest that with an increase in Fe concentration from 0.04 wt% to 0.5 wt%, the rate of the reaction increases steadily, reaching a plateau at 0.5 wt% as shown in Figure 4b. In addition, the turnover rate (TOR), i.e. moles of converted EG normalized *per* moles Fe on the catalyst and *per* unit time, undergoes a steady decline, indicating a decrease in the average Fe-site activity when Fe-loadings are increasing. These results suggest that the active sites are the highly-dispersed Fe species, which form inside the zeolite micropores.[19,21,22,32] Our characterization results further suggest that with Fe content above 0.5 wt%, larger Fe_xO_y-species start dominating the catalyst surface. In addition, we also conducted catalytic tests with $FeCl_3$, and bulk Fe_2O_3. $FeCl_3$, acting as a potential homogeneous "quasi-single Fe-site" catalyst, was active but very unselective, while bulk FeO_x showed minimal amounts of formic acid as product (see Table S4). These results further corroborate that the active species of Fe on the zeolites are the highly dispersed monomeric ones.

Screening of different supports and transition metals: The case for the superior activity and stability of Fe inside MFI

Besides commercial MFI, also Beta Zeolites (BEA) and mordenite (MOR) zeolites were tested for the oxidative cleavage reaction. However, the as-received technical HBEA25 and HMOR20,

although they had Fe impurities (ICP-OES: 0.05 wt%), showed no catalytic activity (Table 2). It is also worth pointing out that the acidity, present in the protonated form of the tested zeolites, does not have any quantifiable effect on the catalytic activity. This was also evident from the very poor performance of the in-home synthesized HMFI50 (conversion < 10%, Table S2). Even after impregnating HBEA25 and HMOR20 with additional 0.5 wt% Fe the catalytic activity was still inferior compared to that of 0.5Fe/HMFI55. This suggests that the MFI structure, having smaller 10-membered ring micropores, probably provides a better confinement for preferential formation of small monomeric Fe-sites.[42] On the other hand, the BEA and MOR type structures having bigger 12-membered ring pores facilitate the formation of undesired FeO_x aggregates.[43] We also tested SiO_2 and Al_2O_3 as supports with 0.5 wt% of Fe, which showed no activity at all, further underlining the need for structured microporous environment as it is the case in the zeolites.

Apart from Fe, other metals in the 1st row of transition metals, are known to catalyze oxidative transformations, also with hydrogen peroxide as the oxidizing agent.[17,18,21,29] Therefore, we screened a wide range of transition metals, namely V, Cr, Ti, Cu, Ag, Co, Mn and Ni. For the screening procedure, we used 0.5 wt% of metal on HBEA25 as support, because in contrast to HMFI55 it had no intrinsic activity (Table 2). Among all metals, only Fe and Cr showed considerable activity for the oxidative cleavage of EG to formic acid (Table S5). However, in the case of 0.5Cr/HBEA25 we observed extensive leaching of Cr-species into the aqueous solution, indicated by a strong violet coloration of the solution after contacting 0.5Cr/HBEA25 with H_2O_2. The violet color suggests the formation of the CrO_5 peroxo species, which can be generated by oxidation of chromates with H_2O_2.[44] A hot filtration test was conducted for the reaction where 0.5Cr/HBEA25 catalyst was used, in which the conversion continued to increase even after separating the solid catalyst (see Figure S8). This suggests strong leaching of Cr in the solution, which was also confirmed by ICP-OES analysis of the filtered reaction solution. Based on the collected results, Fe/MFI are the most active and stable catalysts for the oxidative cleavage of EG.

Table 2. Catalytic oxidative cleavage of EG using different zeolites as well as SiO_2 and Al_2O_3 supports impregnated with 0.5 wt% Fe. Reaction conditions: $n_{EG} = 0.715$ mmol; $n_{H2O2} = 3.6$ mmol; $V_{H2O} = 10$ ml; $m_{cat} = 100$ mg; $T = 323$ K, reaction time = 5 h.

Entry	Catalyst	Conversion [%][a]	Yield [%][a]	Selectivity [%][a]
1	HMFI55	72.2	57.1	79.1
2	HBEA25	0	0	–
3	HMOR20	0	0	–
4	0.5Fe/HMFI55	100	47.7	47.7
5	0.5Fe/HBEA25	54.1	24.3	45.0
6	0.5Fe/HMOR20	35.1	5.4	15.5
7	0.5Fe/SiO₂	2.4	0	0
8	0.5Fe/Al₂O₃	3.1	0	0

[a] According to HPLC.

ChemCatChem

Full Papers
doi.org/10.1002/cctc.202200993

**Chemistry
Europe**
European Chemical
Societies Publishing

Catalyst stability and reusability

The stability and reusability of the Fe/HMFI55 catalyst was also investigated. For this, 0.5Fe/HMFI55 was tested and it showed little to no conversion after separation *via* hot filtration (Figure 5a), suggesting that the catalytically active sites are of heterogeneous nature. In addition, we also studied the reusability of the catalyst, where the used catalyst was only dried in air at 363 K for 16 h. The conversion was also limited to 70% to better investigate the catalyst before reaching full conversion. Owing to the good stability of the Fe-catalyst, the activity and selectivity could be preserved for three consecutive runs (see Figure 5b). A slight decrease in conversion in the third run could be due to catalyst mass loss after each separation process and possible deposition of carbonaceous species over the active sites, which could not be desorbed during the intermediate treatment between runs.

Beyond providing the most active and stable catalytic sites for this transformation, Fe is also the most abundant metal in nature and is less toxic. According to the American Insitute of Chemical Engineers (AIChE) we can attribute a high sustainability index to this process when considering stability, reusability and abundance of the catalyst in combination with mild reaction conditions, water solvent and green H_2O_2 oxidant.[10]
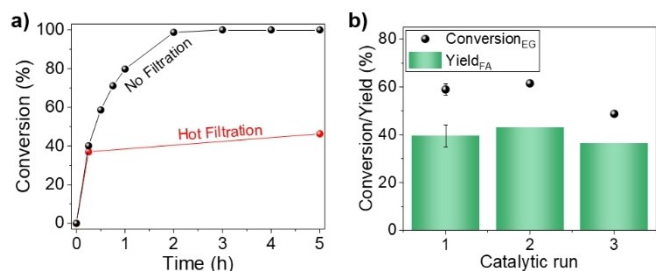
Correlation of catalytic activity with the nature of Fe-sites

The characterization results evidenced that below 0.5 wt% of Fe the majority of the species are present as monomeric species. Catalytic activity, on the other hand, increased with Fe-loading only up to 0.5 wt%, point from which it plateaued (Figure 4). To better display the dominant active sites in the oxidative cleavage of EG over Fe/MFI catalysts, the correlation of the catalytic activity with the type of the Fe-sites, derived from the UV-vis analysis, is shown in Figure 6. TOR shows a positive correlation to the relative amount of monomeric Fe-sites. This dependence on monomeric sites is also reported by recent literature on Fe/MFI systems for the methane oxidation reaction.[21,22] Indeed, when Luo *et al.*[22] studied the Fe/MFI catalyzed methane oxidation, also using H_2O_2, they found a similar linear correlation between the proportional amount of monomeric Fe-sites and the product yield per amount of Fe. *In-situ* Raman studies by Hammond et al. revealed that the oxidation of methane with H_2O_2 over dimeric Fe-sites on their Fe/MFI leads to the formation of monomeric Fe-sites (Fe–OOH), which were speculated to be the active oxidizing sites.[31] In addition, we also observed a negative correlation of the TOR with oligomeric Fe-sites and bulk Fe_2O_3 (Figure 6b). Therefore, we conclude that the optimal catalysts should have well distributed monomeric Fe-sites and no/minimal amount of oligomeric/bulk Fe species, which have no major contribution to the catalytic activity and may even be detrimental as they may block accessibility to the active surface area inside the zeolite.

Figure 5. a) Hot filtration experiment compared to regular reaction (no filtration) over time on 0.5Fe/HMFI55. Catalyst was separated after 0.25 h for hot filtration test. b) Catalyst activity in three consecutive runs. Reaction time for each run was 0.5 h. Reaction conditions: $n_{ethylene\ glycol} = 0.715$ mmol; $n_{H2O2} = 3.6$ mmol; $V_{H2O} = 10$ ml; $m_{cat} = 100$ mg; T = 323 K.

Reaction mechanism

We used EG (**1**) as model compound to investigate the reaction mechanism of the oxidative cleavage of vicinal diols over Fe/MFI catalysts. During product analysis *via* HPLC of the oxidative cleavage of EG on 0.5Fe/HMFI55 over time, we detected small amounts (< 1% selectivity) of glycolic aldehyde (**2**), glyoxal (**3**), glycolic acid (**4**) and oxalic acid (**7**), indicating possible intermediates with fast kinetics for their oxidation. Additionally, we analyzed the gas phase of the reaction products *via* micro GC (reactor shown in Figure S9), where we detected CO_2 and CO in a ratio of 1 to 0.7. Considering all the reaction products in solution and gaseous phase, we were able to nearly close the carbon balance, which leads us to assume that formation of carbonaceous species deposited on the zeolite are negligible. In several control experiments, we investigated compounds **2**, **3**, **4** and **7** as well as glyoxylic acid (**5**), another possible intermediate,[45] as starting materials for the oxidative cleavage. We observed that compounds **2**, **3**, **4** and **5** are fully converted to formic acid (**6**) under reaction conditions. EG (**1**) only reaches a conversion of 70%, indicating that the initial alcohol oxidation of **1** is the rate determining step (RDS) of the reaction. Further,
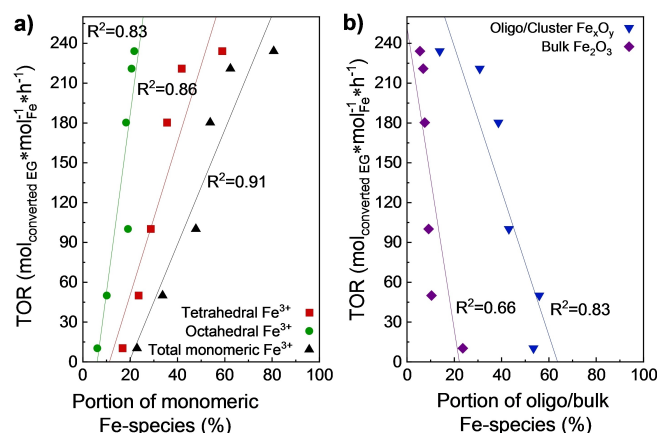
Figure 6. Linear correlation between activity and relative amount of a) monomeric Fe-sites, and b) oligomeric Fe_xO_y and bulk Fe-sites.

ChemCatChem

Full Papers
doi.org/10.1002/cctc.202200993

Chemistry
Europe
European Chemical
Societies Publishing

for the compounds **2**–**5** we only detected **6** via HPLC analysis, probably due to fast conversion of the any intermediate molecules. When using **6** as starting material, we observed a full conversion to CO and CO_2, without any products detected by HPLC. During the oxidative cleavage of **1** we could observe that the yield of **6** increases over time. However, the yield of **6** decreases when **1** is fully converted, leading us to assume that the over-oxidation of **6** to CO and CO_2 is the primary reason for a decreased selectivity. Compound **7** reached a conversion of 19%, with no observable liquid products in HPLC, leading to assume that only CO and CO_2 were produced. This makes the formation of **7** during the reaction undesirable. To further investigate the role of the catalyst in this reaction mechanism, we also conducted test experiments on molecules **1**–**7** without catalyst. For compounds **1**, **2**, **4** and **6** no conversion was observed when the Fe/MFI catalyst was not present, indicating that oxidation of an alcohol group or the decomposition of **6** only proceeds on the Fe/MFI catalyst. However, for molecules **3** and **5** full conversion is detected even without the presence of the catalyst and only in contact with H_2O_2. Here, **6** was the only product detected. Notably, the conversion of **3** without any catalyst leads to formation of **6** in very high selectivity of 96%, while the uncatalyzed conversion of **5** only leads to moderate selectivity of 35%. This strongly indicates, that the C—C bond in compound **3** is cleaved in a way that produces two equivalents of **6** without formation of CO or CO_2, while cleavage of the C—C bond in **5** leads to the formation of at least one equivalent of CO or CO_2. It is known in the literature, that the α-bond of α-keto carboxylic acids, like compound **5**, can be cleaved with H_2O_2 with the formation of CO_2.[46] Due to the catalyzed oxidative cleavage of **1** leading to selectivity of **6** close to 80%, we assume that the actual C—C bond cleavage does not proceed over the formation of compound **5** and a C—C bond cleavage for intermediate **3** or **4** is more likely. Based on these findings, we propose the mechanism as shown in Figure 7. At first, oxidation of one of the alcohol groups on EG (**1**) to an aldehyde **2** can occur, which we propose to be the RDS. The second oxidation could happen on the other alcohol or the newly formed aldehyde group, leading to two possible intermediates, **3** or **4**. Oxidation of one of the aldehyde groups on **3** or oxidation of the alcohol group of the glycolic acid now leads to the formation of **5**, which is likely to be cleaved into **6** or to be oxidized into **7**. Formation of **7** is undesired because its conversion only leads to CO and CO_2. The most prominent side reaction is the over-oxidation of formic acid to CO and CO_2, which is primarily responsible for selectivities below 100%. The fact that a catalyst is needed for the alcohol oxidation step, as well as that all intermediates only appear in small amounts during the course of the reaction, suggests that the initial alcohol oxidation of **1** is the rate-limiting step. Notably the proposed mechanism resembles the mechanism found in the metabolic conversion of **1**, catalyzed partially by alcohol-dehydrogenase[47] containing Fe as one of their active metals, while molecular oxygen is used as the oxidizing agent.[48]

Broadening the scope of Fe/MFI as oxidative catalysts for bio-derived molecules

To demonstrate the versatility of the Fe/MFI catalyst we tested several vicinal diols as substrates for the oxidative cleavage reaction. For this, we tested 1,2 vicinal diols with varying alkyl chain length (1,2-propane diol, 1,2-butane diol, 1,2-hexane diol), which represent possible bio-derivable diol molecules.[49]

Additionally, we also tested biomass platform molecules containing vicinal diol functions, like glycerol, sorbitol and D-glucose. The main product formed was always FA, with lower amounts ($< 23\%$) of higher carboxylic acids formed in some of
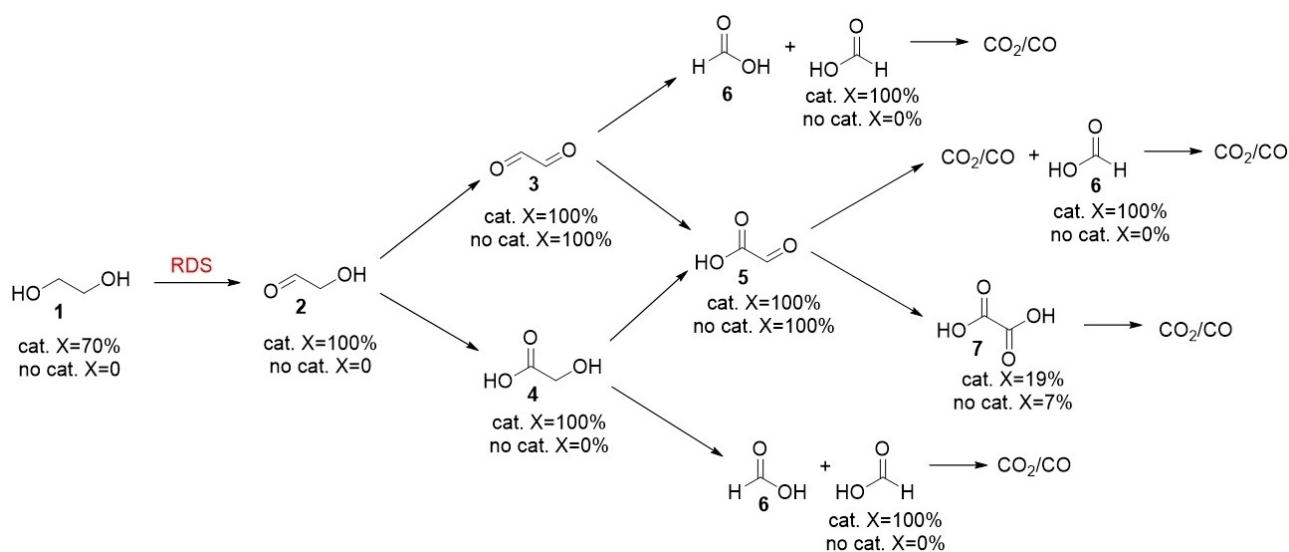

Figure 7. Proposed mechanism of oxidative cleavage of EG and the plausible reaction intermediates. Molecules **1**, **2**, **3**, **4**, **6** and **7** were identified by HPLC. CO_2 and CO were identified by micro-GC. RDS = Rate determining step. Cat. = catalyzed reaction; uncat. = uncatalyzed reaction. Reaction conditions: $n_{EG} = 0.715$ mmol; $n_{H2O2} = 3.6$ mmol; $V_{H2O} = 10$ ml; $m_{HMFI55} = 100$ mg; T = 323 K, reaction time = 5 h.

ChemCatChem

Full Papers
doi.org/10.1002/cctc.202200993

**Chemistry
Europe**
European Chemical
Societies Publishing

the cases (Table 3). The Fe/HMFI catalyst investigated here in presence of H_2O_2 as oxidant, was indeed active in the oxidative cleavage of all tested substrates containing vicinal diol groups. This is an exciting result, considering that this catalyst is potentially able to convert a mixture of bio-derived vicinal diols without prior separation yielding FA selectively, which could make such oxidative cleavage process more economically viable. Upon increase in C-chain length, we observe a decrease in reaction rate. This could be due to the lower accessibility of the bulkier molecules into the active Fe-sites inside the zeolite micropores. Further, when long-chain carboxylic acids are formed, eg., valeric acid (Entry 4), conversion of this acid to BA, AA and mainly FA was observed, probably due to a decarboxylation process which decreases the acid chain length by one carbon atom at a time, releasing CO_2 in the process.[50]

Conclusion

This study demonstrated the unprecedented use of Fe/MFI catalysts in the oxidative cleavage of vicinal diols. To investigate the catalytic performance as well as the active sites of Fe/MFI in detail, we used ethylene glycol (EG) as a model substrate, yielding 2 equivalents of formic acid in very high selectivity ($X_{formic\ acid} = 80\%$; $S_{formic\ acid} = 89\%$). The reaction was conducted using the green oxidant H_2O_2 in an aqueous medium at ambient pressure, allowing for easy and green process. Among several transition metals tested in the reaction, Fe showed the highest activity and stability. The other zeolite and oxide supports tested also underperfomed compared to MFI type zeolite support, probably due to its ability to confine Fe-species. Extensive characterization unravelled the major types of Fe-species formed in the Fe/MFI catalysts, where monomeric Fe-sites dominated at lower Fe-loadings, while oligomeric/bulk FeO_x species were in majority for Fe-loadings over 0.5 wt%. Correlation of catalytic acivity with the different Fe-species

revealed that the monomeric Fe-sites confined in the zeolite MFI micropores are the active species for the oxidative cleavage of EG. Observing the kinetics of product formation over time and using control experiments with intermediate molecules as starting materials, we could uncover the reaction mechanism and that the initial alcohol oxidation of EG was the rate determining step. We could also demonstrate that the Fe/MFI catalyst can be used in the oxidative cleavage of other vicinal diols with varying chain length and of bio-derived polyols such as glycerol, sorbitol, glucose with FA as the main product. The applicability of Fe/MFI catalysts to a wide variety of biogenic oxygenates promotes the production of industrially relevant carboxylic acids in a sustainable way. Moreover, results showed the high stability of Fe/MFI catalysts under reaction conditions which did not loose activity over at least 3 reaction cycles. This study also suggests that further improvement to increase the share of monomeric Fe-species in zeolites are needed for improving catalytic performance. Future studies will focus on increasing the accessibility of the bulky reactant molecules to the active sites inside the zeolite micropores. By using abundant, non-noble and non-toxic Fe as catalyst, renewable H_2O_2 as oxidizing agent, and mild reaction conditions, this approach provides new capabilities for the production of valuable chemicals from biomass *via* oxidative cleavage.

Experimental Section

Materials

All reagents were used as received: Tetraethyl orthosilicate (>99%, Alfa Aesar), Tetrapropylammonium hydroxide (40%, Sigma Aldrich), $Al(NO_3)_3 \cdot 9H_2O$ and NaOH (Merck). SiO_2 (63-200 μm), $Cu(NO_3)_2 \cdot 3H_2O$, $Co(NO_3)_2 \cdot 6H_2O$ (>99%) (Fluka), Al_2O_3 (90 standardized), $Fe(NO_3)_3 \cdot 9H_2O$ (Merck), $Ti(iPrOH)_4$ (97%) and $VO(acac)_2$ (≥99%) (Thermo Fisher Scientific), $Mn(NO_3)_2 \cdot 6H_2O$ (98%, Alfa Aesar), $Ni(NO_3)_2 \cdot 6H_2O$ (99.9%, abcr), $Cr(NO_3)_3 \cdot 9H_2O$, $AgNO_3$ (VWR). H_2O_2 (30%, Merck), Ethylene glycol (>99%, Alfa Aesar), Glycerol (≥99.5%, Honeywell), Sorbitol (>99.5%), 1,2-Hexane diol (>97%) (Fluka), D-glucose (anhydrous, VWR), 1,2-propane diol (98%), 1,2-Butane diol (98%) (Sigma Aldrich), 1,2-Cyclohexane diol (≥98%, Thermo Fisher Scientific). Glycol aldehyde, glyoxal (40%), glyoxylic acid (Sigma Aldrich), glycolic acid (≥99.5%, Merck), formic acid (≥99%, VWR). Commercial HMFI55, HBEA25 and HMOR20 were supplied by Clariant.

Catalyst preparation

Hydrothermal synthesis for HMFI50 was carried out based on a method published by Mintova et al.[33] TEOS, 40% TPAOH, NaOH, $Al(NO_3)_3 \cdot 9H_2O$ and H_2O were stirred overnight at RT to ensure complete hydrolyzation of the alcohols. The resulting gel composition was $0.125\ Na_2O : 0.05\ (TPA)_2O : 0.02\ Al_2O_3 : 1.0\ SiO_2 : 100\ H_2O$. The mixture was then transferred to a Teflon-lined stainless steel autoclave and heated to 443 K for 36 h. Crystallized products were separated by centrifuge (4900 r/min, 15 min), washed with deionized H_2O, dried at 343 K and calcined at 823 K (5 K/min) for 12 h, to completely remove the organic template. The NaHMFI50 was then transformed into NH_4MFI50 *via* three consecutive ion exchanges with NH_4NO_3 (0.1 M, 12 h) and finally calcined at 550 K (5 K/min) for 4 h in static air to obtain HMFI50.

Table 3. Conversion of different bio-available substrates and yield of formic acid during oxidative cleavage reactions over 0.5Fe/HMFI55. Reaction conditions: $n_{substrate} = 0.715$ mmol; $n_{H2O2} = 1.8$ mmol per carbon atom of the substrate; $V_{H2O} = 10$ ml; $m_{cat} = 100$ mg; $T = 323$ K, reaction time = 2 h.

Entry	Substrate	Conversion [%][a]	Selectivity [%][a]
1	Ethylene glycol	99	FA: 52
2	1,2-Propane diol	61	FA: 54
			AA: 23
3	1,2-Butane diol[b]	99	FA: 54
			AA: 10
			PA: 10
4	1,2-Hexane diol[b]	62	FA: 26
			AA: 19
			PA: 3
			BA: Traces
			VA: 2
5	Glycerol[c]	86	FA: 48
6	Sorbitol[c]	36	FA: 25
7	D-Glucose[b,c]	49	FA: 18

[a] Conversion and selectivity derived from HPLC analysis. [b] $T = 353$ K. [c] Selectivity was normalized to amount of C atoms in substrate. FA=Formic acid; AA=Acetic acid; PA: Propionic acid; BA: Butyric acid; VA=Valeric acid.

The 0.5Fe/HMFI55 catalysts were prepared *via* an incipient wetness impregnation method. The desired amount of metal precursor was dissolved in an amount of H_2O or ethanol corresponding to the pore volume. Subsequently, the solution was added dropwise to the zeolite powder and mixed with a spatula until the entire solution was added. The resulting mixture was then dried at 343 K and calcined at 773 K (5 K/min) for 4 h in static air.

Characterization methods

Powder X-Ray diffraction (XRD) experiments were performed using a diffractometer (X'Pert Pro, PANalytical) with a Bragg-Brentano geometry and Cu—Kα radiation (1.54060 Å). The diffractograms were recorded from 5° to 120° (2θ), with a step size of 0.017° (0.53 s acquisition time).

Elemental analysis was carried out *via* inductively coupled plasma atomic emission spectroscopy (ICP-OES). The zeolite samples were digested in a mixture of aqua regia and hydrofluoric acid and treated with microwave radiation (2 h, 500 W) before measurements.

Specific surface area, as well as pore volume of the zeolites were examined by determination of nitrogen-physisorption isotherms. Samples were first pre-treated at 623 K for 4 h in vacuum. Afterwards, nitrogen was adsorbed at 77 K using a NOVATouch gas sorption analyzer (Anton Paar). The specific surface area was determined according to the Brunauer-Emmett-Teller (BET) method via multipoint measurements.

Ultraviolet-visible spectroscopy (UV-vis) of the samples were measured on an Agilent instrument in diffuse reflection on a quartz window between the wavelengths of 200 nm and 800 nm. Spectralon was used as a reference. The reflectance was used to calculate the K/S coefficient ratios following the Kubelka-Munk theory, with K being the absorption coefficient, S being the back-scattering coefficient and R being the measured reflectance.

$$\frac{K}{S} = \frac{(1-R)^2}{2R}$$

The UV-vis spectra were deconvoluted by applying four Gaussian curves at 210, 278, 360, 510 nm and fitting for least squares using Origin Pro 2019.

Scanning electron microscopy (SEM) analyzes were performed with a LEO Gemini 982 from Zeiss (Oberkochen, Germany) at 3.5–5.0 keV equipped with an annular high brightness in-lens-SE detector for high resolution and true surface imaging.

Transmission electron microscopy (TEM) was performed on carbon covered copper grids using catalyst powders. For TEM measurements, the catalyst powders were mounted onto a standard lacey carbon TEM grid (S166 3). Subsequently, the samples were examined using a ThermoFischer Themis 300 (S)TEM aberration corrected electron microscope operated at 300 keV. High angle annular dark field (HAADF) scanning transmission electron microscopy (STEM) images were acquired with a Super-X EDS detector.

Conventional XAS (X-ray absorption spectroscopy) at the Fe K-edge (7112 eV) was measured at the P65 beamline[51] at Deutsches Elektronen-Synchrotron (DESY, Hamburg, Germany) in fluorescence mode (step scanning collection). Samples with low Fe-loading (HMFI55 to 0.5Fe/HMFI55) were measured as self-supporting pellets (13 mm in diameter), while higher loadings (1.0Fe/HMFI55 and 5.0Fe/HMFI55) were measured as pellets diluted with cellulose to adjust the absorption. α-Fe_2O_3 (hematite) as reference sample was measured in transmission mode. For energy selection, a Si(111)

crystal monochromator was used. Measurements were taken between an energy range of 7000 to 7900 eV. Fluorescence spectra were collected with a four element Ge detector and Kα₁ and Kα₂ lines were considered. The beam size was 0.5 mm × 1 mm (V × H).

In-situ XAS experiments were conducted at the CATACT beamline[52] at the KIT light source in fluorescence mode (step scanning collection). For energy selection, a Si(111) crystal monochromator was used. Measurements were taken between an energy range of 7000 to 7900 eV. A silicon drift detector was used to detect and select the emitted radiation in fluorescence at the maximum of the Fe $K_{\beta 1,3}$ emission line (e.g., at 7058.81 eV). The beam size was 0.3 mm × 1.2 mm (V × H). For all collected spectra XAS data reduction (energy calibration, background removal and normalization) was carried out using the Demeter software packages including the Athena code (version 0.9.26).[53] μ(E) data were transformed to EXAFS χ(k) data, in which the k-range from 2 to 10 was Fourier transformed into R-space (k-weighting of 3).

Catalytic reactions

Catalytic tests were conducted in a round bottom flask under atmospheric pressure. 0.715 mmol substrate was added to a 50 ml flask, dissolved in 10 ml H_2O and 5 eq. of H_2O_2 was added to the solution at once. The flask was covered with a rubber septum, heated to the desired temperature in an oil bath and stirred at 1000 rpm. For kinetic experiments, 0.5 ml of liquid were sampled with a syringe and filtered through a 0.45 μm filter to separate the catalyst. After the desired reaction time, the flask was quickly cooled in an ice bath and the catalyst was separated *via* syringe filtration (0.45 μm).

For hot filtration tests, liquid aliquot was taken after 40–50 % conversion while the temperature of the reaction medium was still at 323 K. For the catalysts re-usability study, consecutive test reactions were performed, between which the catalyst was separated *via* centrifugation and dried overnight at 363 K in air, before re-use. We aimed at a reaction time that led to a conversion below 70 %, to investigate the catalyst activity before reaching maximum conversion. The resulting product solution was analyzed *via* high-performance liquid chromatography (HPLC). HPLC analysis were carried out using a Hitachi Primaide, Bio-Rad Aminex HPX-87H column, with 5 mM H_2SO_4 eluent, at 298 K and 88 bar.

[1] C. H. Christensen, J. Rass-Hansen, C. C. Marsden, E. Taarning, K. Egeblad, *ChemSusChem* **2008**, *1*, 283–289.

[2] N. Wilde, J. Přech, M. Pelz, M. Kubů, J. Čejka, R. Gläser, *Catal. Sci. Technol.* **2016**, *6*, 7280–7288.

[3] J. van Haveren, E. L. Scott, J. Sanders, *Biofuels. Bioprod. Bior.* **2008**, *2*, 41–57.

[4] a) L. Malaprade, *Bull. Soc. Chim. Fr.* **1934**, *3*, 833–852; b) R. Criegee, *Ber. Dtsch. Chem. Ges.* **1931**, *64*, 260–266.

[5] E. Farnetti, C. Crotti, *Catal. Commun.* **2016**, *84*, 1–4.

[6] S. Maerten, C. Kumpidet, D. Voß, A. Bukowski, P. Wasserscheid, J. Albert, *Green Chem.* **2020**, *22*, 4311–4320.

[7] E. Amadio, R. Di Lorenzo, C. Zonta, G. Licini, *Coord. Chem. Rev.* **2015**, *301–302*, 147–162.

[8] J. Hietala, A. Vuori, P. Johnsson, I. Pollari, W. Reutemann, H. Kieczka in *Ullmann's Encyclopedia of Industrial Chemistry.* Vol. 6 ed., Wiley-VCH, Weinheim, Germany, **2016**.

[9] F. Shen, R. L. Smith Jr., J. Li, H. Guo, X. Zhang, X. Qi, *Green Chem.* **2021**, *23*, 1536–1561.

[10] P. Saavalainen, S. Kabra, E. Turpeinen, K. Oravisjärvi, G. D. Yadav, R. L. Keiski, E. Pongrácz, *J. Chem.* **2015**, *2015*, 1–12.

[11] a) S. Wang, D. E. Doronkin, M. Hähsler, X. Huang, Di Wang, J.-D. Grunwaldt, S. Behrens, *ChemSusChem* **2020**, *13*, 3243–3251; b) A. Velazquez Abad, P. E. Dodds, *Energ. Policy* **2020**, *138*, 111300.

[12] a) S. Yang, A. Verdaguer-Casadevall, L. Arnarson, L. Silvioli, V. Čolić, R. Frydendal, J. Rossmeisl, I. Chorkendorff, I.E. L. Stephens, *ACS Catal.* **2018**, *8*, 4064–4081; b) S. Czioska, A. Boubnov, D. Escalera-López, J. Geppert, A. Zagalskaya, J. Röse, E. Saraçi, V. Alexandrov, U. Krewer, S. Cherevko, J.-D. Grunwaldt, *ACS Catal.* **2021**, *11*, 10043–10057; c) R. Dittmeyer, J.-D. Grunwaldt, A. Pashkova, *Catal. Today* **2015**, *248*, 149–159.

[13] A. Wang, H. Jiang, *J. Org. Chem.* **2010**, *75*, 2321–2326.

[14] a) T. Mizugaki, K. Kaneda, *Chem. Rec.* **2019**, *19*, 1179–1198; b) F. Liao, T. W. B. Lo, D. Sexton, J. Qu, C.-T. Wu, S. C. E. Tsang, *Catal. Sci. Technol.* **2015**, *5*, 887–896.

[15] EuChemS, "Element Scarcity - EuChemS Periodic Table - EuChemS", to be found under https://www.euchems.eu/euchems-periodic-table/, **2022**.

[16] a) S. Kal, S. Xu, L. Que, *Angew. Chem. Int. Ed.* **2020**, *59*, 7332–7349; b) K. D. Sutherlin, B. S. Rivard, L. H. Böttger, L. V. Liu, M. S. Rogers, M. Srnec, K. Park, Y. Yoda, S. Kitao, Y. Kobayashi, M. Saito, M. Seto, M. Hu, J. Zhao, J. D. Lipscomb, E. I. Solomon, *J. Am. Chem. Soc.* **2018**, *140*, 5544–5559.

[17] M. Høj, M. J. Beier, J.-D. Grunwaldt, S. Dahl, *Appl. Catal. B-Environ.* **2009**, *93*, 166–176.

[18] D. E. Doronkin, A. Y. Stakheev, A. V. Kucherov, N. N. Tolkachev, M. Kustova, M. Høj, G. N. Baeva, G. O. Bragina, P. Gabrielsson, I. Gekas, S. Dahl, *Top. Catal.* **2009**, *52*, 1728–1733.

[19] E. J. M. Hensen, Q. Zhu, R. A. van Santen, *J. Catal.* **2003**, *220*, 260–264.

[20] G. D. Pirngruber, J.-D. Grunwaldt, J. A. van Bokhoven, A. Kalytta, A. Reller, O. V. Safonova, P. Glatzel, *J. Phys. Chem. B* **2006**, *110*, 18104–18107.

[21] T. Yu, Z. Li, W. Jones, Y. Liu, Q. He, W. Song, P. Du, B. Yang, H. An, D. M. Farmer, C. Qiu, A. Wang, B. M. Weckhuysen, A. M. Beale, W. Luo, *Chem. Sci.* **2021**, *12*, 3152–3160.

[22] T. Yu, Y. Su, A. Wang, B. M. Weckhuysen, W. Luo, *ChemCatChem* **2021**, *13*, 2766–2770.

[23] a) X. Yu, B. Wu, M. Huang, Z. Lu, J. Li, L. Zhong, Y. Sun, *Energy Fuels* **2021**, *35*, 4418–4427; b) A. Oda, K. Aono, N. Murata, K. Murata, M. Yasumoto, N. Tsunoji, K. Sawabe, A. Satsuma, *Catal. Sci. Technol.* **2022**, *12*, 542–550.

[24] a) T. Franken, A. Heel, *J. CO2 Util.* **2020**, *39*, 101175; b) Z. Yang, H. Li, H. Zhou, L. Wang, L. Wang, Q. Zhu, J. Xiao, X. Meng, J. Chen, F.-S. Xiao, *J. Am. Chem. Soc.* **2020**, *142*, 16429–16436; c) J. H. Yun, R. F. Lobo, *J. Catal.* **2014**, *312*, 263–270; d) L.-C. Wang, Y. Zhang, J. Xu, W. Diao, S. Karakalos, B. Liu, X. Song, W. Wu, T. He, D. Ding, *Appl. Catal. B-Environ.* **2019**, *256*, 117816; e) J. Kirchner, Z. Baysal, S. Kureti, *ChemCatChem* **2020**, *12*, 981–988.

[25] a) M. M. Diallo, S. Laforge, Y. Pouilloux, J. Mijoin, *Catal. Lett.* **2018**, *148*, 2283–2303; b) N. Sobuś, I. Czekaj, *Catal. Today* **2022**, *387*, 172–185.

[26] a) E. V. Kondratenko, J. Pérez-Ramírez, *Appl. Catal. A-Gen.* **2004**, *267*, 181–189; b) G. M. Lari, C. Mondelli, J. Pérez-Ramírez, *ACS Catal.* **2015**, *5*, 1453–1461; c) S. Schlicher, N. Prinz, J. Bürger, A. Omlor, C. Singer, M. Zobel, R. Schoch, J. K. N. Lindner, V. Schünemann, S. Kureti, M. Bauer, *Catalysts* **2022**, *12*, 675.

[27] H. T. Luk, C. Mondelli, S. Mitchell, D. Curulla Ferré, J. A. Stewart, J. Pérez-Ramírez, *J. Catal.* **2019**, *371*, 116–125.

[28] S. Abelló, D. Montané, *ChemSusChem* **2011**, *4*, 1538–1556.

[29] A. Boubnov, H. W. P. Carvalho, D. E. Doronkin, T. Günter, E. Gallo, A. J. Atkins, C. R. Jacob, J.-D. Grunwaldt, *J. Am. Chem. Soc.* **2014**, *136*, 13006–13015.

[30] a) X. Cui, H. Li, Y. Wang, Y. Hu, L. Hua, H. Li, X. Han, Q. Liu, F. Yang, L. He, X. Chen, Q. Li, J. Xiao, D. Deng, X. Bao, *Chem.* **2018**, *4*, 1902–1910; b) B. E. R. Snyder, L. H. Böttger, M. L. Bols, J. J. Yan, H. M. Rhoda, A. B. Jacobs, M. Y. Hu, J. Zhao, E. E. Alp, B. Hedman, K. O. Hodgson, R. A. Schoonheydt, B. F. Sels, E. I. Solomon, *P. Natl. Acad. Sci. USA* **2018**, *115*, 4565–4570; c) B. E. R. Snyder, P. Vanelderen, M. L. Bols, S. D. Hallaert, L. H. Böttger, L. Ungur, K. Pierloot, R. A. Schoonheydt, B. F. Sels, E. I. Solomon, *Nature* **2016**, *536*, 317–321.

[31] C. Hammond, I. Hermans, N. Dimitratos, *ChemCatChem* **2015**, *7*, 434–440.

[32] J. Pérez-Ramírez, A. Gallardo-Llamas, *Appl. Catal. A-Gen.* **2005**, *279*, 117–123.

[33] Y. Shen, Z. Qin, S. Asahina, N. Asano, G. Zhang, S. Qian, Y. Ma, Z. Yan, X. Liu, S. Mintova, *J. Mater. Chem. A* **2021**, *9*, 4203–4212.

[34] M. Schwidder, M. Kumar, K. Klementiev, M. Pohl, A. Bruckner, W. Grunert, *J. Catal.* **2005**, *231*, 314–330.

[35] J. Wang, H. Xia, X. Ju, Z. Feng, F. Fan, C. Li, *J. Catal.* **2013**, *300*, 251–259.

[36] K. Feng, H. Zhang, J. Gao, J. Xu, Y. Dong, Z. Kang, J. Zhong, *Appl. Phys. Lett.* **2020**, *116*, 191903.

[37] A. Boubnov, A. Roppertz, M. D. Kundrat, S. Mangold, B. Reznik, C. R. Jacob, S. Kureti, J.-D. Grunwaldt, *Appl. Surf. Sci.* **2016**, *386*, 234–246.

[38] T. E. Westre, P. Kennepohl, J. G. DeWitt, B. Hedman, K. O. Hodgson, E. I. Solomon, *J. Am. Chem. Soc.* **1997**, *119*, 6297–6314.

[39] A. Boubnov, H. Lichtenberg, S. Mangold, J.-D. Grunwaldt, *J. Synchrotron Radiat.* **2015**, *22*, 410–426.

[40] G. D. Pirngruber, P. K. Roy, R. Prins, *Phys. Chem. Chem. Phys.* **2006**, *8*, 3939–3950.

[41] P. Marturano, L. Drozdová, A. Kogelbauer, R. Prins, *J. Catal.* **2000**, *192*, 236–247.

[42] B. E. R. Snyder, M. L. Bols, H. M. Rhoda, D. Plessers, R. A. Schoonheydt, B. F. Sels, E. I. Solomon, *Science (New York, N. Y.)* **2021**, *373*, 327–331.

[43] a) J. Zhang, X. Tang, H. Yi, Q. Yu, Y. Zhang, J. Wei, Y. Yuan, *Appl. Catal. A-Gen.* **2022**, *630*, 118467; b) S. Campisi, C. Palliggiano, A. Gervasini, C. Evangelisti, *J. Phys. Chem. C* **2019**, *123*, 11723–11733.

[44] P. S. Charalampidis, P. Veltsistas, S. Karkabounas, A. Evangelou, *Eur. J. Med. Chem.* **2009**, *44*, 4162–4168.

[45] a) B. Mückschel, O. Simon, J. Klebensberger, N. Graf, B. Rosche, J. Altenbuchner, J. Pfannstiel, A. Huber, B. Hauer, *Appl. Environ. Microbiol.* **2012**, *78*, 8531–8539; b) J. Schnaidt, M. Heinen, Z. Jusys, R. J. Behm, *J. Phys. Chem. C* **2013**, *117*, 12689–12701.

[46] A. A. Vlessis, D. Bartos, D. Trunkey, *Biochem. Bioph. Res. Co.* **1990**, *170*, 1281–1287.

[47] R. K. Scopes, *FEBS Lett.* **1983**, *156*, 303–306.

[48] a) K. L. Clay, R. C. Murphy, *Toxicol. Appl. Pharm.* **1977**, *39*, 39–49; b) J. Brent, *Drugs* **2001**, *61*, 979–988.

[49] K. Tomishige, Y. Nakagawa, M. Tamura in *Production of Platform Chemicals from Sustainable Resources*, Springer, Singapore, **2017**.

[50] A. Olmedo, J. C. D. Río, J. Kiebist, R. Ullrich, M. Hofrichter, K. Scheibner, A. T. Martínez, A. Gutiérrez, *Chem. Eur. J.* **2017**, *23*, 16985–16989.

[51] E. Welter, R. Chernikov, M. Herrmann, R. Nemausat, *AIP Conf. Proc.* **2019**, *1*, 040002.

[52] A. Zimina, K. Dardenne, M. A. Denecke, D. E. Doronkin, E. Huttel, H. Lichtenberg, S. Mangold, T. Pruessmann, J. Rothe, T. Spangenberg, R. Steininger, T. Vitova, H. Geckeis, J.-D. Grunwaldt, *Rev. Sci. Instrum.* **2017**, *88*, 113113.

[53] B. Ravel, M. Newville, *J. Synchrotron Radiat.* **2005**, *12*, 537–541.